Role of NBI fuelling in contributing to density peaking between the ICRH and NBI identity plasmas on JET

OPEN ACCESS
IOP Publishing | International Atomic Energy Agency Nuclear Fusion
Nucl. Fusion **62** (2022) 066008 (18pp) https://doi.org/10.1088/1741-4326/ac5667

Role of NBI fuelling in contributing to density peaking between the ICRH and NBI identity plasmas on JET

T. Tala[1,*], F. Eriksson[2], P. Mantica[3], A. Mariani[4], A. Salmi[1], E.R. Solano[5], I.S. Carvalho[6], A. Chomiczewska[7], E. Delabie[2], J. Ferreira[6], E. Fransson[8], L. Horvath[2], P. Jacquet[2], D. King[2], A. Kirjasuo[1], S. Leerink[9], E. Lerche[10], C. Maggi[2], M. Marin[11], M. Maslov[2], S. Menmuir[2], R.B. Morales[2], V. Naulin[12], M.F.F. Nave[6], H. Nordman[8], C. Perez von Thun[7], P.A. Schneider[13], M. Sertoli[14], K. Tanaka[15] and JET Contributors[a]

[1] VTT, PO Box 1000, FI-02044 VTT, Espoo, Finland
[2] CCFE, Culham Science Centre, Abingdon, OX14 3DB, United Kingdom of Great Britain and Northern Ireland
[3] Institute for Plasma Science and Technology, CNR, Milano, Italy
[4] Department of Physics 'G. Occhialini', University of Milano-Bicocca, Milano, Italy
[5] CIEMAT, Av. Complutense 40, Madrid 28040, Spain
[6] Instituto de Plasmas e Fusão Nuclear, Universidade de Lisboa, Lisboa, Portugal
[7] IPPLM, Warsaw, Poland
[8] Chalmers University of Technology, Göteborg, Sweden
[9] Aalto University, Espoo, Finland
[10] LPP-ERM/KMS, TEC Partner, Brussels, Belgium
[11] DIFFER, Eindhoven, The Netherlands
[12] Danish Technical University Physics, Lyngby, Denmark
[13] Max-Planck-Institut für Plasmaphysik, Boltzmannstraße 2, 85748 Garching, Germany
[14] Tokamak Energy Ltd, 173 Brook Drive, Milton Park, Oxfordshire, OX14 4SD, United Kingdom of Great Britain and Northern Ireland
[15] National Institute for Fusion Science, Toki, Gifu, Japan

E-mail: tuomas.tala@vtt.fi

Received 11 June 2021, revised 14 February 2022
Accepted for publication 17 February 2022
Published 30 March 2022

Abstract

Density peaking has been studied between an ICRH and NBI identity plasma in JET. The comparison shows that 8 MW of NBI heating/fueling increases the density peaking by a factor of two, being $R/L_n = 0.45$ for the ICRH pulse and $R/L_n = 0.93$ for the NBI one averaged radially over $\rho_{tor} = 0.4, 0.8$. The dimensionless profiles of q, ρ^*, υ^*, β_n and $T_i/T_e \approx 1$ were matched within 5% difference except in the central part of the plasma ($\rho_{tor} < 0.3$). The difference in the curvature pinch (same q-profile) and thermo-pinch ($T_i = T_e$) between the ICRH and NBI discharges is virtually zero. Both the gyro-kinetic simulations and integrated modelling strongly support the experimental result where the NBI fuelling is the main

[*] Author to whom any correspondence should be addressed.
[a] See Joffrin *et al* 2019 (https://doi.org/10.1088/1741-4326/ab2276) for the JET Contributors.

contributor to the density peaking for this identity pair. It is to be noted here that the integrated modeling does not reproduce the measured electron density profiles, but approximately reproduces the difference in the density profiles between the ICRH and NBI discharge. Based on these modelling results and the analyses, the differences between the two pulses in impurities, fast ions (FIs), toroidal rotation and radiation do not cause any such changes in the background transport that would invalidate the experimental result where the NBI fuelling is the main contributor to the density peaking. This result of R/L_n increasing by a factor of 2 per 8 MW of NBI power is valid for the ion temperature gradient dominated low power H-mode plasmas. However, some of the physics processes influencing particle transport, like rotation, turbulence and FI content scale with power, and therefore, the simple scaling on the role of the NBI fuelling in JET is not necessarily the same under higher power conditions or in larger devices.

Keywords: density peaking, NBI fuelling, particle transport, particle transport modelling, dimensioness identity plasma

(Some figures may appear in colour only in the online journal)

1. Introduction

Research on particle transport plays a crucial role in the achievement of practical fusion energy. Since fusion power scales with the square of the density ($P_{fus} \sim n^2$), obtaining high values of the central density in a reactor is of particular importance. Reaching very high density is only possible with peaked density profiles, indicating that particle transport and density peaking studies indeed deserve a lot of attention. This point is underlined, for example in conceptual studies for a future power plant, where densities are required to exceed the empirical Greenwald density limit by a factor of 1.2 to 1.5 [1]. Electron and ion particle transport, partly due to its complexity in tokamaks, has received less attention than the heat transport channels [2]. There is an on-going activity in the ITPA group on understanding particle transport for ITER, with the emphasis on the three following topics: electron and mixed-ion particle transport, isotope scaling and density peaking. This paper addresses the particular aspect of density peaking.

Earlier database studies in JET, AUG and C-Mod showed that density peaking scales with several plasma parameters, the most dominant ones being collisionality, Greenwald fraction and NBI fueling [3–5]. The database studies in references [3–5] all emphasized the dominant role played by the collisionality in affecting density peaking. However, there are other type of particle transport analyses performed in JET that are clearly indicating the importance of the particle sources [6–9]. Previous theory and modelling papers have already reviewed possible key mechanisms affecting core electron density peaking [2, 10]. What is challenging in JET is that the temperature ratio T_i/T_e and NBI source (heat and particles) are strongly correlated, but at the same time their influence on density peaking is expected to be opposite [11]. As a consequence, this correlation between density peaking and the source could always have been disturbed or biased in all the previous database analyses and therefore, the role of NBI fueling in contributing to density peaking could not have been estimated correctly. To unambiguously estimate the relative roles of different factors affecting density peaking, one has to separate the effect of transport and fueling from each other. In this paper, this will assess this by executing a dimensionless identity experiment between the ICRH and NBI heated discharge where NBI fueling can ideally be separated.

Core density profile peaking and particle transport have been recently studied on several tokamaks [12–14]. In these experiments, the contribution to density peaking due to NBI fueling versus inward particle pinch was found be quite different, varying roughly between 10%–50%. This indicates that different plasma operational conditions and plasma turbulence regimes can affect the role of NBI fueling on the electron density peaking observed in tokamaks. NBI fueling was found to be the major player (∼50%) or even dominant in JET NBI heated discharges in contributing to density peaking in a dimensionless collisionality experiment at all υ^* values [12]. On the contrary, DIII-D has shown that the inward pinch contributes most to density peaking [13]. Similarly to DIII-D, AUG has observed that NBI fueling is only a minor player in influencing density peaking [14]. However, one must note here that the experimental conditions are not exactly comparable between the devices and therefore, no generalization is possible. As the JET result was quite different from the AUG and DIII-D ones, it deserved a more refined experiment to quantify the role of NBI fueling in density peaking.

A stationary density profile is provided by a balance of outward diffusion and inward convection, driven by either neoclassical or turbulent mechanisms, and by the NBI particle source. There are neutral particles entering the plasma from the scrape-off-layer. However, this edge neutral particle source is usually small or even negligible in the core plasma ($r/a < 0.8$) in JET. This result is supported by the edge fueling and edge particle transport studies by means of the gas puff modulation technique in JET [15] and the neutral fueling can be neglected at $r/a < 0.8$. A general feature of particle transport

in the core of a tokamak plasma is that core particle sources are small but not negligible as most tokamak discharges at least on larger devices have NBI fueling in the core. Here we report the experiment where we compare an ICRH discharge with zero core particle source to an NBI fueled one.

Gas modulation technique will be exploited here as additional data to quantify any difference in particle transport between the ICRH and NBI heated plasmas. This technique has been used in many devices in the past, for example in AUG [16], JET [17], DIII-D [18], W7-AS [19] and LHD [20] and much more recently on JET [12] and DIII-D [13]. The local electron density response to the gas injection was measured with high resolution Thomson scattering (HRTS) diagnostics [21] close to the outer midplane. Density modulation amplitudes below 1% (in the core) are reliably measured thus allowing us to have minimal plasma disturbance and further with long plasma discharges, reduced error bars in the Fourier analysis of the perturbative particle transport coefficients. It is worth noting here that this paper is devoted to electron particle transport, as we can have the modulated data for electrons and also the diagnostics capabilities support that. However, recently it has been reported in JET that the ion particle transport can in fact have quite a different characteristics [22, 23].

There are earlier studies in comparing the NBI heated and fuelled plasmas with either ECRH or ICRH heated plasmas, i.e. scans to study the role of NBI fueling and density peaking although no clean dimensionless identity pair has been performed or presented so far. In JET, an experiment where a discharged with 11 MW of NBI power was compared to another discharge with 8 MW of ICRH power +2 MW of NBI power showed similar results to the one presented in this paper in the global confinement, i.e. the ICRH dominated discharge had some 10% higher confinement, higher pedestal density and lower density peaking [24]. On AUG, adding ECRH power on top of the NBI heated plasma increases the central density peaking, but in the core region $0.4 < r/a < 0.8$, no difference in the density profile is observed [25]. Similar observations where only the central density is affected by the addition or change of ECRH or ICRH to the baseline NBI heating is further reported in high collisionality plasma [26] and low collisionality plasma [27] on AUG. On DIII-D, density peaking was studied by changing the NBI torque from co- to counter injected direction, and the highest density peaking was observed in the counter-NBI plasma due to higher inward particle pinch [28].

In this paper, we aim to quantify the role of NBI fueling in contributing to density peaking in JET by executing identity discharges between the ICRH and NBI heated plasmas. By first executing the ICRH discharge with maximum ICRH power available in JET H-mode discharge, the target of the NBI heated counter-part discharge will be to match the dimensionless plasma profiles of q, ρ^*, υ^*, β_n and T_i/T_e of the ICRH discharge. This identity also includes to achieve as similar equilibrium as possible, and with the same shape. In an ideal situation, the pair would be so identical that any difference in the density peaking could be directly attributed to the influence of the NBI fueling. However, in real experiment, in addition to the obvious desired difference in core particle source, for example the plasma rotation, fast ion (FI) content, impurities and edge pedestal properties may not be the same between the NBI-ICRH pair. It has been reported that rotation or $E \times B$ shearing [29] and FIs [30] can have an influence on density peaking, and thus, any difference between the ICRH-NBI pair must be quantified. Both the ICRH and NBI discharges are complemented with gas puff modulation so that we can extract the perturbative particle transport coefficients for each discharge. By performing dimensionally matched identity plasmas, in addition to learning about particle transport and NBI fueling, we can also study how the different heating systems and their effects in the plasma affect plasma confinement, MHD, impurities, radiation, pedestal, ELMs and the gas puff modulation properties.

Various modelling efforts will complement the experimental studies on density peaking. The main goal of the modelling is twofold; on one hand to quantify what role of NBI fuelling is in contributing to density peaking compare and on the other hand to quantify how similar the background transport is between the ICRH and NBI identity pulses. Density peaking could also be influenced by changes in particle transport between the two discharges, for example due to different rotation or FI content, thereby they could either enhance or reduce the pure NBI fueling effect on density peaking that can be seen directly in the experimental steady-state density profiles. The gyrokinetic (GK) simulations and integrated transport modelling will be performed to strengthen the experimental conclusions on the importance of NBI fuelling in influencing density peaking. This dataset also serves as a very good basis on an extensive and thorough particle transport model validation efforts.

The paper is organized as follows. Section 2 is devoted to showing the experimental conditions on which the identity pair is based. The operation issues and global parameters are compared to quantify the identity. The detailed experimental comparison is presented in section 3. This includes various kinds of comparison of plasma profiles, density peaking, and also the pedestal and MHD activity. The GK simulations and full profile modelling are presented in section 4. The main scope is to refine and further verify the experimental results by comparing the particle transport between the ICRH and NBI pulses. Finally, the results are summarized in section 5 with conclusions.

2. NBI and ICRH identity plasma in JET H-mode conditions

The identity experiment between the ICRH and NBI heated plasmas is far from trivial to achieve. For example the dominant heating channel can be different, and in that case matching the dimensionless profiles between the electron and ion heated discharges would be impossible. Moreover, the H-mode threshold can be different, the power deposition profiles can have a different shape, making the temperature profiles inevitably different. What concerns particularly JET is that the ICRH power could be limited to values below the H-mode threshold. Our target is to match the profiles in the core region,

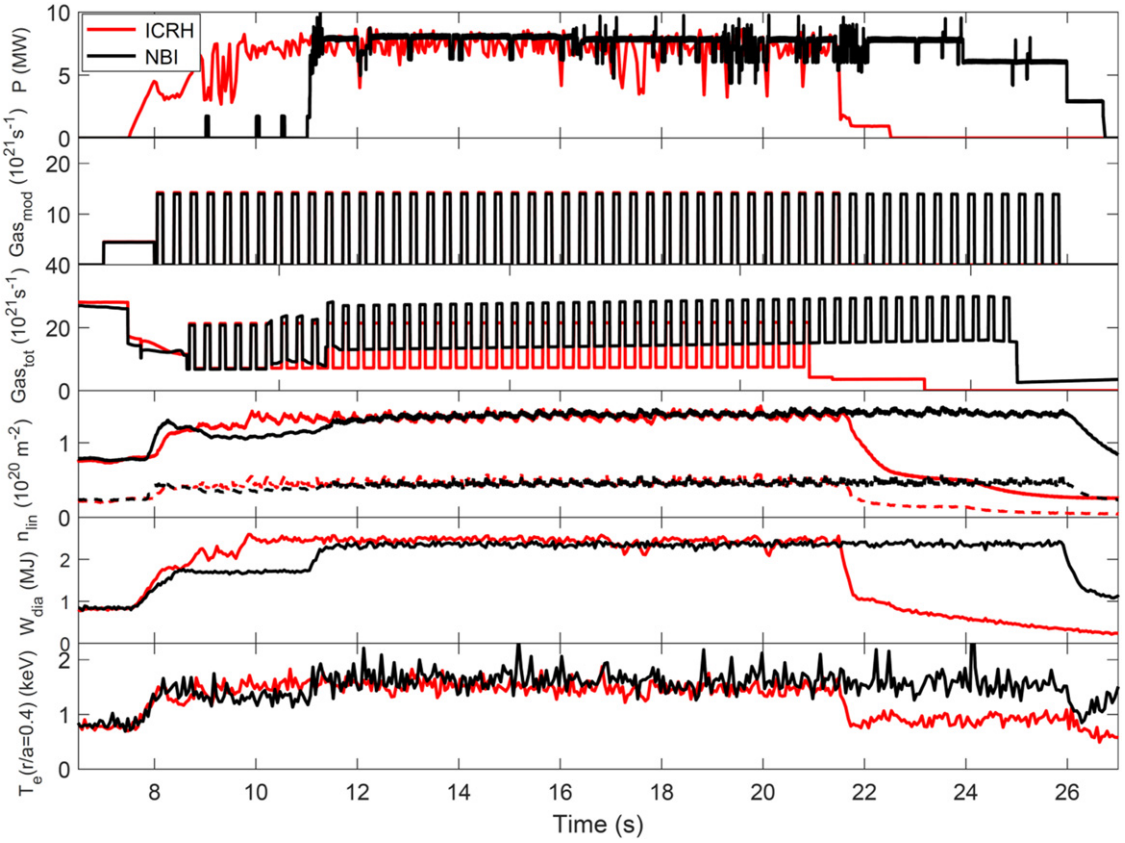

Figure 1. Key time traces of the ICRH (red, #95097) and NBI (black, #95272) discharges. The solid lines in the fourth frame from above correspond to the central interferometer chord and the dashed lines correspond to the edge interferometer chord, respectively.

i.e. our region of interest is the so-called confinement region at $0.4 < \rho_{\rm tor} < 0.8$ where matching is easier as most of the heating takes place in the central region at $\rho_{\rm tor} < 0.4$. A detailed descriptions of the JET ICRH and the NBI systems can be found in references [31, 32], respectively.

However, despite all the challenges, we executed the NBI-ICRH identity experiment. Up to 15 s long H-mode plasmas with 8 MW of ICRH power were achieved. This in fact resulted in JET record high injected ICRH energy of 108 MJ. The ICRH discharges, using the H minority heating scheme at 3% minority concentration, were stationary without any major MHD activities or impurity accumulation. The ICRH power stayed more or less stationary for the whole length of the discharge and independent of the gas puff modulation even if the gas puff modulation time trace can be seen in the coupling resistance of the ICRH antenna. The NBI heated counter-part discharges were executed consecutively with the target to match the dimensionless plasma profiles of q, ρ^*, υ^*, $\beta_{\rm n}$ and $T_{\rm i}/T_{\rm e}$ of the ICRH discharge with as similar equilibrium as possible and with the same shape. There is not very much freedom to maneuver the NBI source radially in JET to control the power deposition profiles.

The time traces of the key parameters for the best matched ICRH-NBI pair are shown in figure 1. The electron temperature and density traces are similar between the ICRH and NBI discharges at 8 MW power. The diamagnetic energy is about 5% higher for the ICRH discharge. Both pulses had gas puff modulation at 3 Hz throughout the discharges to extract perturbative particle transport coefficients as illustrated in figure 1. The local electron density response to the vessel top gas injection was measured with HRTS diagnostics [21] close to the outer mid-plane. Density modulation amplitudes of a few % in the core were measured as seen clearly also in the interferometer signal in figure 1 (fourth frame from above). The solid lines correspond to the central interferometer chord and the dashed lines correspond to the edge interferometer chord, respectively. On top of the modulated gas puff, stationary gas puff was needed for both pulses, and due to different edge and SOL conditions, the NBI discharge required more stationary gas to sustain similar pedestal density. The reason for the need of more stationary gas puff in the case of the NBI pulse originates from the different ELM characteristics, i.e. the NBI discharge has more regular large size type I ELMs flushing particles out of the plasma to SOL than the ICRH one. The influence of ELMs on density profile is, however, limited to the region $\rho_{\rm tor} > 0.8$, and therefore, for the core transport studies in the confinement region, this is not playing an important role, which was also reported in earlier similar particle transport studies [12]. More details on the ELMs and MHD are in section 3 around figure 7.

The success in obtaining the identity plasma between the ICRH and NBI pulses is characterised in figure 2 where the main dimensionless and dimensional profiles are compared. All the profiles (except the ion temperature profile for the

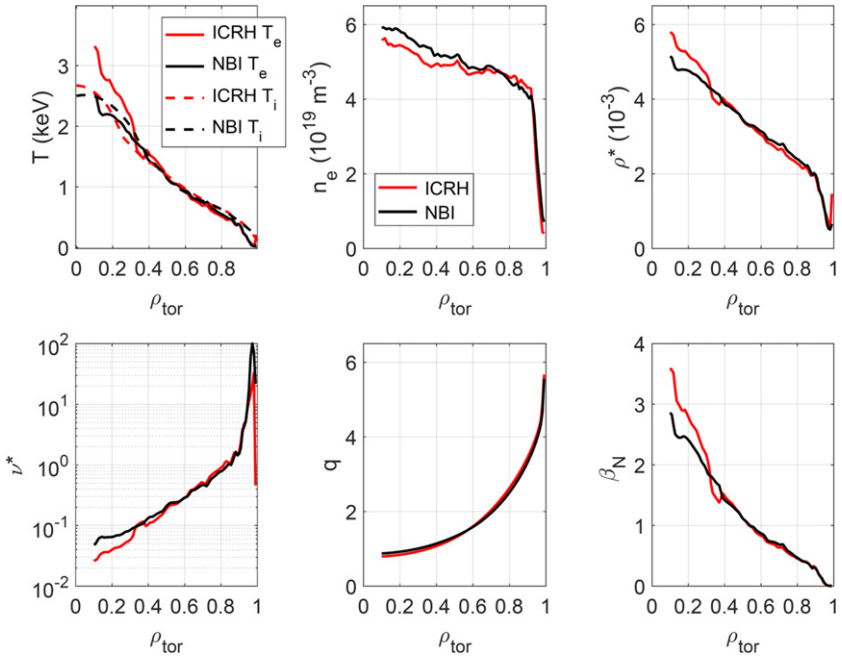

Figure 2. Comparison of the main dimensionless and dimensional plasma profiles between the ICRH (#95097, red traces) and NBI (#95272, black traces) discharges as a function of the normalized toroidal flux co-ordinate defined as ($\rho_{\rm tor} = \sqrt{\frac{\phi}{\pi B_0}\phi_{\rm edge}{}^{-1}}$).

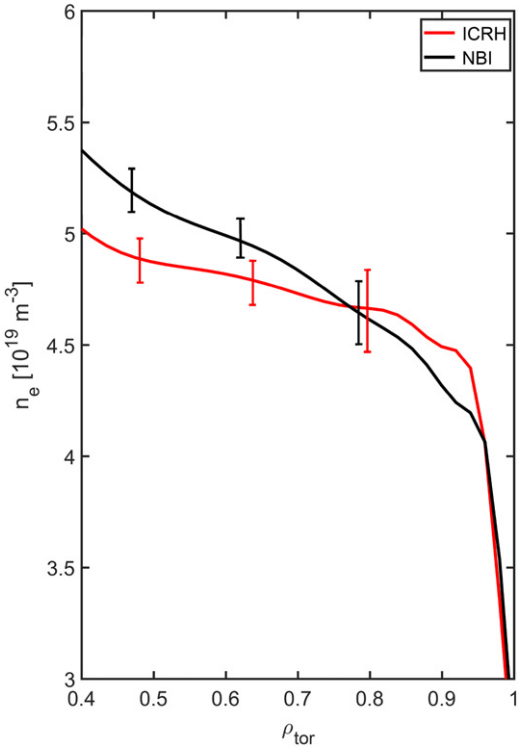

Figure 3. Radially zoomed density profiles (time-averaged, implying ELM averaging and fitting) of the ICRH heated (#95097) and NBI heated (#95272) discharges.

ICRH case) are time averaged over $t = 15$–16 s. These profiles are independent of the chosen time window or the length of it, indicating the genuinely stationary character of the discharges. The dimensionless profiles of q, ρ^*, ν^*, $\beta_{\rm n}$ and $T_{\rm i}/T_{\rm e} \approx 1$ were matched within 5% difference except in the central part of the plasma ($\rho_{\rm tor} < 0.3$) where the ICRH discharge has higher electron temperature than the NBI one. ν^* is defined as $\nu^* = 17 n_{\rm e} e^2 R_0^{2.5} q_{95} / 12\pi^{1.5}\varepsilon_0^2 T_{\rm e}^2 a^{1.5}$. ν^* is used as a local quantity in figure 2, but in table 1 it is a global value, based on volume averaged density and temperature. The ion temperature is measured with CXRS diagnostics using the NBI blips in the ICRH discharge [33], and therefore, it is not a time averaged profile as the other profiles. After careful analysis and validation of the NBI blip data, there is no difference within the measurement accuracy of around 5% between $T_{\rm i}$ and $T_{\rm e}$ at least $\rho_{\rm tor} > 0.3$, which is illustrated in figure 2 (upper left frame). Also for the NBI pulse, $T_{\rm i}$ equals $T_{\rm e}$ everywhere in the confinement region as shown in figure 2. The ratio of the electron–ion thermal equilibration time to energy confinement time is less than 1/3 for each discharge, supporting the strong electron–ion coupling and the experimentally measured ratio of $T_{\rm i}/T_{\rm e} = 1$. This greatly simplifies our analysis as we can assume that $T_{\rm i}/T_{\rm e} = 1$ is valid everywhere and similarly $T_{\rm ICRH} = T_{\rm NBI}$ in the core or confinement region ($0.4 < \rho_{\rm tor} < 0.8$). Therefore, $T_{\rm i}$ or $T_{\rm e}$ profile or their gradients cannot contribute to any difference observed between the ICRH and NBI discharges. From the turbulence transport point of view, it is also important that the differences in q and magnetic shear are very small if any. The q-profiles have been calculated both with EFIT using the Faradays' constrains and EFIT with pressure constrains. While the different EFIT runs produce different q-profiles themselves, there is no measurable difference in the q-profiles between NBI and ICRH discharges provided that the same type of EFIT constrains are used. Therefore, at least from the theoretical point of view [2] we have succeeded to minimize the difference in the curvature pinch (same q-profile) and thermo-pinch ($T_{\rm i}/T_{\rm e} = 1$ and $T_{\rm ICRH} = T_{\rm NBI}$) between the ICRH and NBI shots, simplifying greatly our main task to

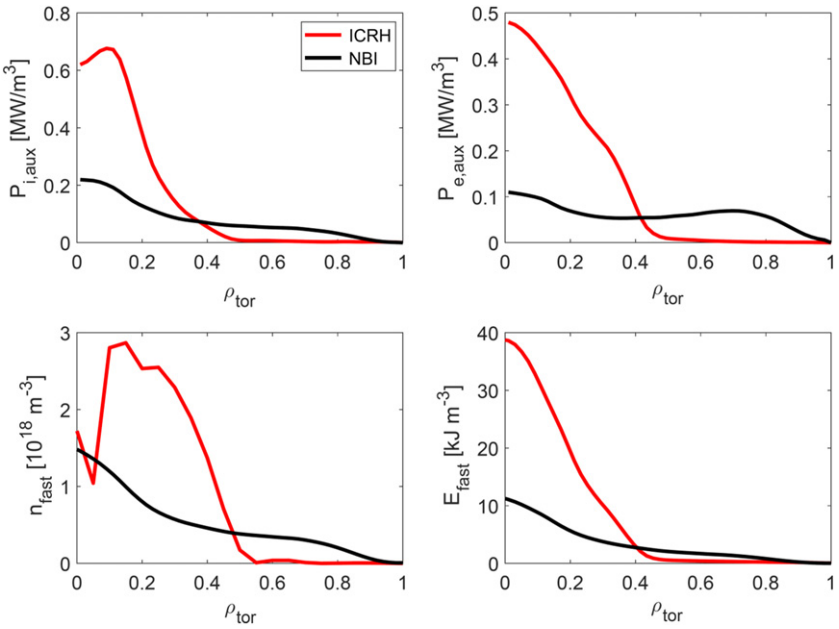

Figure 4. Comparison of the power deposition profiles of ions (top left), electrons (top right) and the FI density (bottom left) and energy (bottom right) between the ICRH heated (red) and the NBI heated (black) discharges, using PION and TRANSP/NUBEAM, respectively.

quantify the role of the NBI fueling in contributing to density peaking in JET.

The most significant difference is the density profile which is a factor of 2 more peaked for the NBI discharge than for the ICRH discharge as is shown in figure 3. Density peaking here is defined as the density gradient length R/L_n, and it has been calculated averaging radially over $\rho_{tor} = 0.4$-0.8 resulting in $R/L_n = 0.93$ for the NBI shot and $R/L_n = 0.45$ for the ICRH shot. However, any other definition for density peaking would result in a similar factor of 2. The profiles have been time averaged over 10 s stationary phase at time interval $t = 11$–21 s and finally fitted using the GPR technique [34]. This procedure implies in practice also ELMs averaging and thus, the density profiles represent here the averaged steady-state density profiles. Within a 2%–3% accuracy, the profiles in figure 3 can be obtained by averaging either for example over 1 s time period instead of the present 10 s time period. This demonstrates that the density profiles are genuinely steady-state profiles and robustly reproducible over long stationary plasma discharges. The error bar calculation is based on more than 200 HRTS data points in 10 s period at each radial position taking into the 3 Hz gas puff modulation affecting ELMs. The resulting error bars are shown in figure 3.

3. Experimental comparison between the NBI and ICRH identity discharges

The main engineering and global dimensionless parameters are compared in table 1. Out of the 8 MW of total heating power roughly 4 MW goes to ions and the other half 4 MW to electrons for both the NBI and the ICRH discharges. This enabled us to achieve $T_e = T_i$ and $T_{ICRH} = T_{NBI}$ at $\rho_{tor} > 0.4$. Larger steady-state gas puff is needed in the NBI pulse to get the same density pedestal height. The confinement is slightly higher ($\sim$10%) in the ICRH case which is mainly due to higher central temperature at $\rho_{tor} < 0.4$. This is originated from the much more peaked power deposition profile. The key differences in table 1 between the two JET discharges are the toroidal rotation (rotation at magnetic axis is 10 km s^{-1} counter-I_p for the ICRH discharge and 110 km s^{-1} co-I_p for the NBI discharge), FI content including the profiles (influencing also β_n), confinement, heavy impurity concentration, radiation and ELM characteristics. The most important differences with their potential influence on particle transport are illustrated later in this paper.

The power deposition profiles and the FI density and energy profiles are compared in figure 4. The NBI power deposition profiles are calculated with NUBEAM code in TRANSP [35–37]. The ICRH power deposition profiles are calculated both with PION [38] and cross-checked with TORIC in TRANSP [39]. As expected, the ICRH power deposition profiles and FI energy and density profiles are more peaked in the center at $\rho_{tor} < 0.4$ than the NBI ones, which, on the other hand, are actually quite flat. This gives rise to higher central electron and ion temperatures at $\rho_{tor} < 0.3$ for the ICRH pulse as shown in figure 2. This is also the main reason for higher β_n and diamagnetic energy observed for the ICRH pulse. Moreover, it also gives rise to higher confinement and H_{98}. For the ICRH pulse, the total integrated power to electrons is 3.8 MW and ions 4.1 MW and the corresponding numbers for the NBI shot are 4.0 MW and 3.9 MW, respectively. This also partly explains why T_i/T_e ratio is close to 1 for each of the discharge at $\rho_{tor} > 0.3$. The role of FIs contributing to transport and density peaking is analyzed and discussed in more detail in section 4.

The power and particle balance analysis of both the ICRH and NBI discharges are illustrated in figure 5. As the ICRH

Table 1. The main engineering and plasma parameters between the ICRH and NBI pulses. B_t and v_{tor} are local values at magnetic axis, the others are global values.

Pulse	95097 (ICRH)	95272 (NBI)
P_{NBI} (MW)	0	8.0
P_{ICRH} (MW)	7.9	0
B_t (T)	2.15	2.15
I_p (MA)	1.8	1.8
τ_E (s)	0.23	0.21
H_{98}	0.8	0.7
P_{rad} (MW)	4	2
Z_{eff}	1.25	1.3
ρ^* (10^{-3})	2.8	2.8
υ^*	0.36	0.36
β_n	1.3	1.1
β_{th}	1.1	1.05
W_{fast}/W_{th}	0.11	0.08
f_{ELM} (Hz)	75	40
$f_{sawtooth}$ (Hz)	2.9	6.0
v_{tor} (km s^{-1})	−10	110

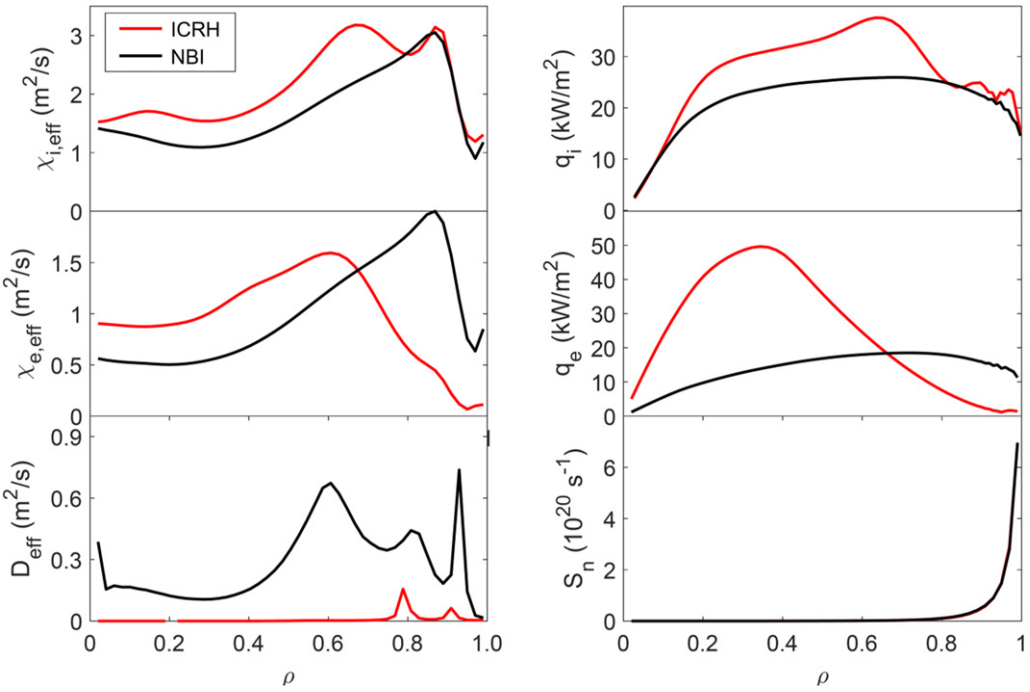

Figure 5. The effective ion, electron and particle diffusion coefficients (left frames) and the ion and electron heat fluxes and the neutral particle source from SOL between the ICRH heated (red) and the NBI heated (black) discharges.

power deposition is more centrally peaked, the heat fluxes of the ICRH pulse are larger in the inner half of the radius. The electron heat fluxes are similar at around $\rho_{tor} = 0.6$ (equal at $\rho_{tor} = 0.65$) between the ICRH and NBI cases. Partly because of this and partly because $\rho_{tor} = 0.6$ is free from the ELM affected area and free from sawtooth affected area, all the following GK analyses will be performed at $\rho_{tor} = 0.6$. The effective particle diffusion coefficients are shown in the bottom left frame and reveal the major difference between the pulses, i.e. the lack of any core particle source in the ICRH case. Therefore, the comparison of effective particle transport coefficients between the ICRH and NBI discharges does not make sense here. The perturbative particle transport coefficients can be determined from the modulated density thanks to the gas puff modulation. However, the perturbative transport coefficients differ from the steady-state particle transport coefficients in these plasmas, for example for the ICRH plasma the perturbative convection is outward while it is evident from the peaked density profile with no core particle source that the steady-state particle convection is inward. This result is dissimilar from the results found in the dimensionless collisionality scan in JET [12] where they were found to be equal. The detailed analysis

of the perturbative transport coefficients is beyond the scope of this paper and is thus left for future work.

The neutral particle sources are calculated with Frantic neutral fluid code inside JINTRAC [40]. We assumed that the energy of the neutral particle at separatrix is 100 eV in the simulations shown in figure 5 (bottom right frame). However, using 300 eV as the energy of the wall-released neutrals does not change simulation results virtually at all, showing that the ionization source inside $\rho_{tor} < 0.8$ is negligible as even the assumption that the energy of the neutral particle at separatrix would be 100 eV is an overestimation. There is no difference in neutral particle profiles between the ICRH and NBI discharges.

A very detailed analysis of impurity composition, Z_{eff} and radiation was performed based on the following diagnostics data: soft x-ray radiation, total radiation from bolometry, tungsten concentration from VUV spectroscopy and Z_{eff} visible Bremstrahlung, together with the kinetic profiles of temperature, density and rotation of the main plasma. The analysis methodology is described in detail in references [41, 42]. The comparison of the ICRH versus NBI discharge with respect to those profiles is illustrated in figure 6. The beryllium density is 20% higher in the plasma center for the NBI discharge, but it is similar in the confinement region at $0.4 < \rho_{tor} < 0.8$. On the other hand, there is a large difference in W density between the pulses, the ICRH pulse having a factor of 6 higher n_W. The nickel density, representing the intermediate charge of plasma impurities, is a factor of 1.5 higher for the NBI pulses than for the ICRH one. These impurity density profiles, while being quite different between the discharges, however, yield similar Z_{eff} profile in the confinement region at $0.4 < \rho_{tor} < 0.8$ while the ICRH pulse has somewhat higher Z_{eff} in the plasma central region. Concerning the radiation profiles, there is an overall factor of about 2 difference between the ICRH and NBI discharges, yielding the total radiation of approximately 4 MW for the ICRH shot and 2 MW for the NBI shot. The radiation in the ICRH discharges originates almost completely from W while for the NBI shot, the radiation contribution from Ni and W are equal, reflecting well the corresponding impurity densities. Higher main chamber radiation in the ICRH discharge is measured by bolometry while the radiation in the divertor region is lower in comparison with the NBI pulse. One can also conclude from this analysis that while the absolute values of impurity densities and radiation are quite different between the pulses, the profile shape of the impurities and radiation is similar. To quantify the possible influence of these different profiles on transport, in particular particle transport and their possible impact on density peaking, detailed modelling activities with GK codes and integrated modelling are needed. This will be reported in section 4.

The MHD and edge pedestal properties between the ICRH and NBI discharges are illustrated in figure 7. We can observe some differences in the MHD activity between the ICRH and NBI discharges in figure 7. The sawtooth activity is present in both pulses, but with a different period. This period determines also the period of other activities, like fish-bones. The sawtooth frequency is 2.9 Hz for the ICRH pulse while it doubles to around 6 Hz for the NBI shot. This is a typical sawtooth behavior in JET. In addition to the sawtooth activity, the ICRH discharge around $t = 15$ s is characterized by fishbone activity with a given frequency span. On the contrary, the NBI pulse is characterized, in addition to sawtooth, by a continuous 1/1 mode (affecting SXR signals), without strong fishbone activity. This is due to the less peaked electron temperature profile. In this pulse one can clearly see a transition from fishbone activity to continuous 1/1 mode when the NBI power is injected around $t = 11$ s, and it is due to the flattening of the electron temperature profile. For the ICRH discharge, weak $n = 1$ neo-classical tearing modes (NTMs) are triggered with a wide frequency span which is an indication of a large hot particle pressure gradient. The NBI discharge on the other hand has weak $n = 1$, $n = 2$ and $n = 3$ NTMs. The effects of all these MHD activities on plasma kinetic profiles is limited to the central region ($\rho_{tor} < 0.3$), and they do not affect the core ($0.4 < \rho_{tor} < 0.8$) transport analysis. Therefore, they are not considered to have an effect on any density peaking related matters in the confinement region. In the central region at $\rho_{tor} < 0.3$, the W concentration and W peaking, in addition to electron temperature profiles, are affected by the sawtooth crashes.

The ELM characteristics between the ICRH and NBI discharges are compared in figure 7. Even if the total absorbed power of 8 MW is the same, the ELMs are quite different. The NBI discharge has more regular ELMs of similar size and most of the ELMs can be counted as type I ELMs. This also results in the NBI pulse having a smaller variation of the line integrated edge density (bottom frame). The ELM characteristics also explains the need of more stationary gas puff in the case of the NBI pulse that originates from the different ELM characteristics, i.e. the NBI discharge has more regular large size type I ELMs flushing particles out of the plasma to SOL than the ICRH one. The ICRH pulse has short ELM free periods ending with a type I ELM, followed by some irregular ELMs. The irregular behavior can be seen in Be II signal, W_{MHD} and the line integrated density traces (three bottom frames in figure 7). The averaged ELM frequencies are 75 Hz and 40 Hz for the ICRH and NBI pulses, respectively, characterized with mixed ELMs and affected by the gas puff modulation. The central temperature trace shows the sawtooth behavior, around 6 Hz for the NBI shot and 3 Hz for the ICRH shot. The time averaged pedestal height is 6%–7% higher for the ICRH discharge as can be seen also in figure 3, and there is also larger time variation in the density pedestal height in the ICRH shot caused by larger ELMs and the ELM free periods. To sum up, the density traces show that the ELM penetration is limited to region $\rho_{tor} > 0.8$ and as a consequence, the difference in the ELM characteristics does not play a significant role for the core particle transport analysis at $0.4 < \rho_{tor} < 0.8$ as the influence of the ELMs is localised at the edge. We do not observe significant either sawtooth or ELM oscillations in the confinement region.

The TRANSP and interpretive JINTRAC analyses of the ICRH versus NBI discharges show that the confinement is a good 10% higher for the ICRH pulse, i.e. $H_{98} \approx 0.8$ and $H_{98} \approx$

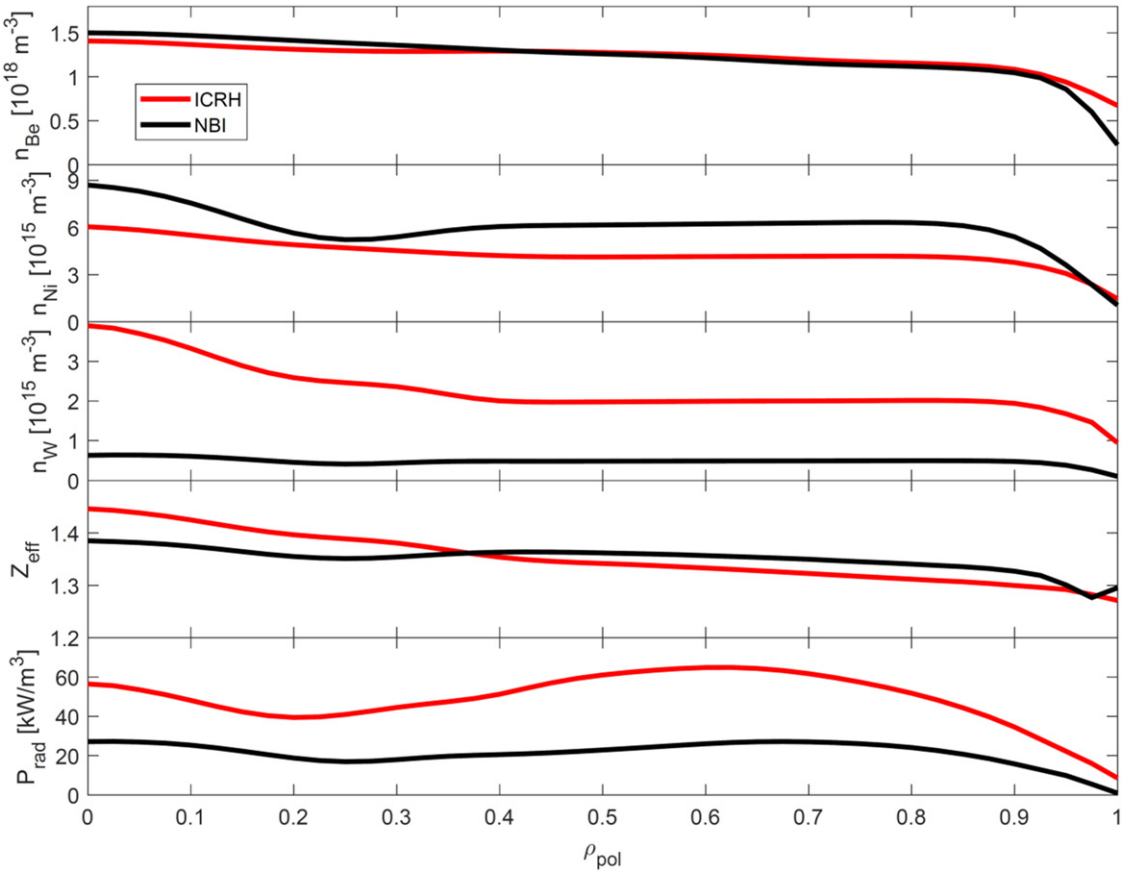

Figure 6. Comparison of the beryllium, nickel and tungsten impurity density profiles, $Z_{\rm eff}$ and the total radiation profiles between the ICRH heated (red) and NBI heated (black) discharges.

Table 2. Main parameters showing a difference in GENE input between ICRH and NBI pulses at the radius of analysis at $\rho_{\rm tor} = 0.6$.

	ICH	NBI
$R/L_{\rm n}$	0.43	0.8
$\gamma_{\rm E}$	−0.02	0.21
$n_{\rm Be}/n_{\rm e}$	0.024	0.024
$R/L_{\rm n,Be}$	0.57	1.07
$n_{\rm Ni}/n_{\rm e}$	9.5×10^{-5}	1.7×10^{-4}
$R/L_{\rm n,Ni}$	−0.27	−0.38
$n_{\rm W}/n_{\rm e}$	4.5×10^{-5}	8.6×10^{-6}
$R/L_{\rm n,W}$	−0.38	−0.41
$n_{\rm FI}/n_{\rm e}$	0	0.0068
$R/L_{\rm n,FI}$	0	2.75
$T_{\rm FI}/T_{\rm e}$	0	20.2
$R/L_{\rm T,FI}$	0	3.55

0.7, respectively. This is due to significantly higher electron and ion temperatures at $\rho_{\rm tor} < 0.3$ in the ICRH pulse which originates from the more central and peaked power deposition profiles, as shown in figure 4. The volume averaged density is 3% higher for the NBI case even if the density pedestal is 5% higher for the ICRH, but this is compensated by the higher density peaking in the NBI discharge. There is around 10% higher thermal energy content in the ICRH case, whereas the total energy content is about 15% higher as the FI fraction to total energy is also higher for the ICRH discharge. Both the increased thermal and total energy content (and the better confinement) in the ICRH discharge originates almost completely (>95%) from the central part inside $\rho_{\rm tor} < 0.4$. This is also visible in the $\beta_{\rm n}$ profile in figure 2 and explains the 20% higher $\beta_{\rm n}$ for the ICRH discharge. The details of these differences are analysed and modelled in section 4. Concerning density peaking, neo-classical ware pinch could be a factor playing a role. However, according to the neo-classical transport code

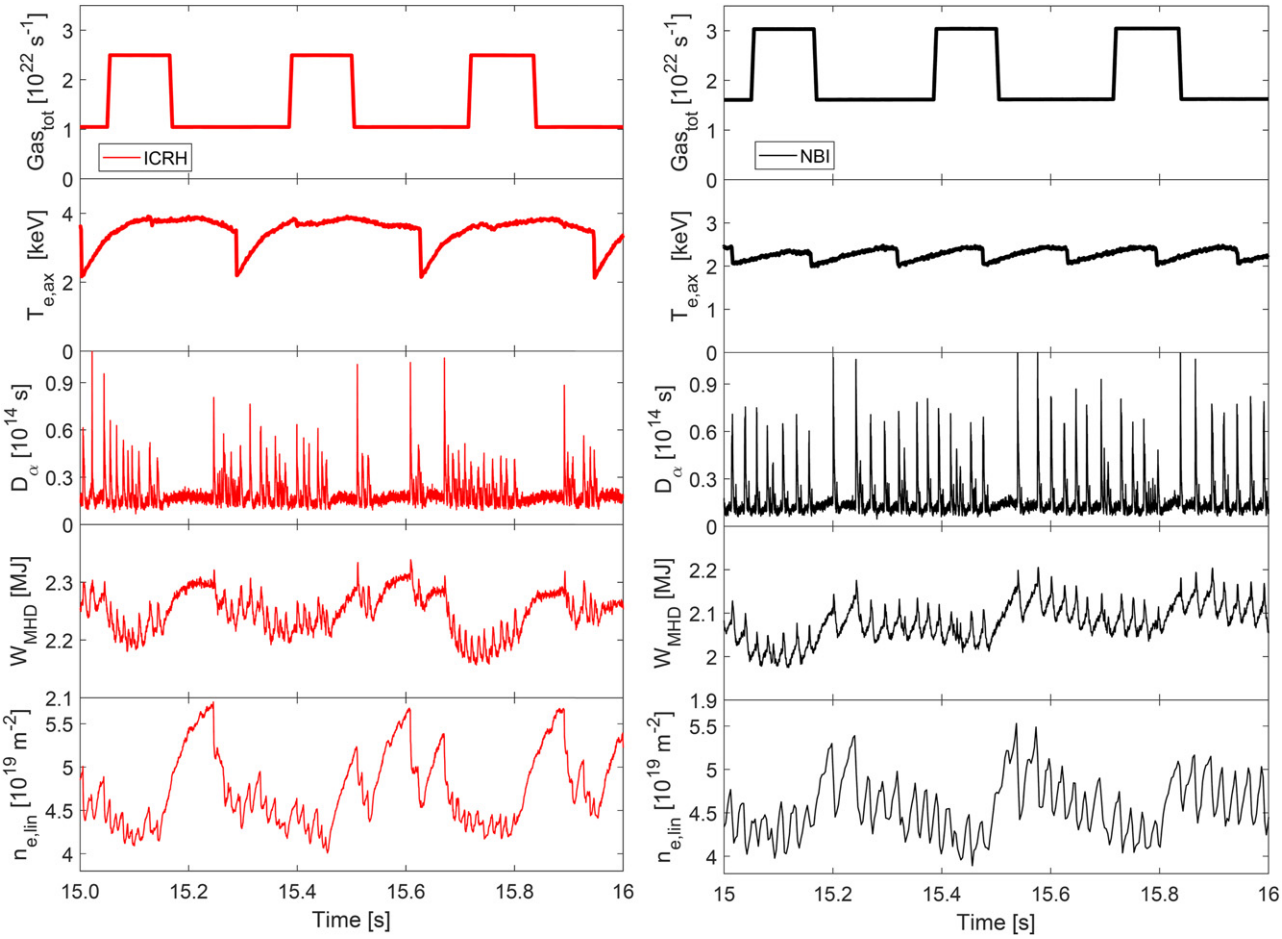

Figure 7. Comparison of the ELM characteristics between the ICRH heated (left frame) and NBI heated (right frame) discharges. Shown are the total gas puffing rate, central T_e, Be II signal, plasma energy and the line integrated density of the edge channel.

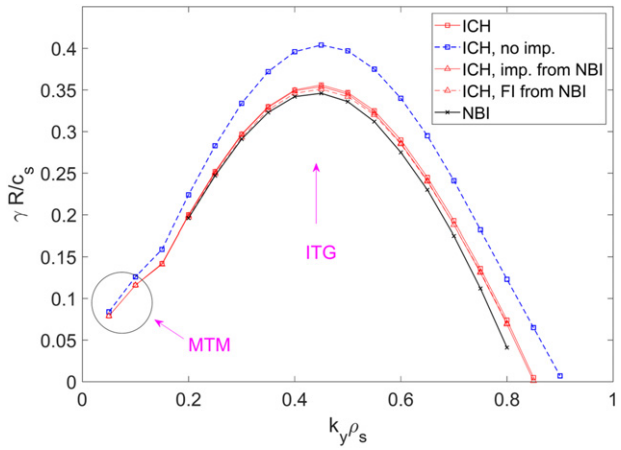

Figure 8. Spectra of the growth rate of the first unstable linear mode as a function of $k_y\rho_s$ when changing parameters starting from the ICRH pulse, and then replacing the impurities and FIs with the ones from the NBI discharge and finally the growth rate of the nominal NBI discharge.

NCLASS [43] calculation, the ware pinch has its maximum value around 0.03 m s^{-1} (inward) for either discharge and therefore, its impact on density peaking is negligible.

Gas puff modulation technique has been developed with high quality time-dependent density profile measurements to determine the perturbed particle transport coefficients on JET [12]. Gas puff modulation was performed with a gas valve at the top of the machine at 3 Hz frequency using rectangular waveform. The modulation rate varied from 0 to 1.4×10^{22} s^{-1} at 30% duty cycle. Typically another gas injection module at the divertor location was used to keep the volume averaged density constant. However, the detailed analysis of the perturbative particle transport and the validation of the gas puff modulation method against the steady-state data presented in this paper is beyond the scope of this paper which is solely based on stationary data and will be referred to a future publication.

4. Gyrokinetic and integrated transport modelling of the ICRH and NBI heated discharges

The main goal of this modelling section is on one hand to quantify what role of NBI fuelling is in contributing to density peaking compare and on the other hand to quantify how similar the background transport is between the ICRH and NBI identity pulses. The key question in this paper is to clarify whether the influence of NBI fuelling on density peaking increase is exactly or closely the difference of the factor of

2 shown in figure 3 or whether the density peaking is also influenced by changes in particle transport between the two discharges. Here we quantify transport with GK simulations using the GENE code [44] and with the quasi-linear (QL) transport model TGLF [45–47], either in stand-alone mode or for integrated transport modelling of plasma profiles using the ASTRA code [48].

Linear and nonlinear ion-scale GK simulations have been performed using the flux-tube (radially local) version of the GENE code at fixed radius $\rho_{tor} = 0.6$. At $\rho_{tor} = 0.6$ the normalized electron density logarithmic gradient R/L_n equals 0.43 for the ICRH case, while it has almost double the value 0.80 for the NBI case, with similar density value $n_e = 5 \times 10^{19}$ m^{-3}. This radius is chosen for the analysis since $T_i = T_e$ for $\rho_{tor} > 0.4$, and moreover FIs coming from the ICRH pulse can be neglected at $\rho_{tor} \geqslant 0.6$, simplifying the comparison between ICRH and NBI pulses. Indeed, summing up, when comparing the GENE input between ICRH and NBI pulses at $\rho_{tor} = 0.6$, in addition to different R/L_n, the only other non-negligible changes in the parameters between the two pulses come from the $E \times B$ rotation shearing, the impurity content and the deuterium FIs from NBI. The similar (almost identical for ICRH and NBI) parameters are the geometrical ones, i.e. the safety factor $q = 1.65$, the shear $\hat{s} = 1.49$, the elongation $\kappa = 1.4$ and the triangularity $\delta = 0.07$, the temperature $T = T_e \sim T_i \sim 0.99$ keV, the corresponding normalized logarithmic gradient $R/L_T \sim 7.6$, the collisionality $\nu_c = 0.0052$ and the ratio of the electron plasma pressure to the magnetic pressure $\beta_e = 2\mu_0 n_e T_e/B_0^2 = 0.0042$, with μ_0 the vacuum permeability and $B_0 = 2.16$ T the vacuum magnetic field on the magnetic axis. The GENE collisional parameter ν_c is used instead of the electron–ion thermal collision rate $\nu_{ei} = 4(n_i/n_e)\sqrt{T_e/m_e}\nu_c/R$, since it depends just on the measured quantities n_e and T_e while ν_{ei} depends on the number of considered species (n_i adapted invoking neutrality). The main plasma parameters that are not identical between the two pulses at $\rho_{tor} = 0.6$ are listed in table 2.

Here, $\gamma_E = -(r/q)(\partial\Omega_{tor}/\partial r)R/c_s$ is the $E \times B$ shearing rate in GENE units, where Ω_{tor} is the toroidal angular velocity and $c_s = \sqrt{T_e/m_i}$ the ion sound speed (note that when $T_e \sim T_i$ is assumed one has $c_s = v_{th,i}$, where $v_{th,i}$ is the ion thermal velocity). The parallel flow shear γ_p was computed consistently with the pure toroidal flow assumption ($\gamma_p \sim -(q/\varepsilon)\gamma_E$, where $\epsilon = r/R$ is the inverse aspect ratio). The impurities, Be, Ni and W, produce very similar effective charges $Z_{eff} = 1.33$ and 1.35 for ICRH and NBI cases, respectively. In the simulations, the heavy impurities (Ni and W) have been merged to compose a single effective species, conserving the effective charge and imposing quasi-neutrality both on density and density gradients, following [49].

The simulations are carried out using realistic geometry, reconstructed using numerical equilibria from EFIT [50, 51], then approximated using a Miller *et al* [52] analytic model, taking into account collisions and finite-β (electromagnetic) effects (from both $B_\perp$ and $B_\parallel$ fluctuations). Linear scans have been performed to evaluate the spectra of the growth rate γ and frequency ω corresponding to the most unstable mode, to characterize the turbulence regimes, at the reference values of the parameters for ICRH and NBI cases. The results are summarized in figure 8. Here, the γ scans are shown, varying physics parameters by starting from the ICRH ones towards the NBI ones. γ is normalized with c_s/R, while the binormal wavenumber k_y with $1/\rho_s$, where $\rho_s = c_s/\Omega_i$ is the ion sound Larmor radius, with Ω_i the ion cyclotron frequency. The ion scales are found to be dominated by the ion temperature gradient (ITG) mode, with micro tearing modes (MTM) which are spotted at the lower wavenumbers. However, MTMs are not found to play a role nonlinearly, therefore they do not impact the nonlinear fluxes. Only the range $0 < k_y\rho_s < 1$ is shown for clarity, since only these wavenumbers are found *a posteriori* to non-negligibly contribute to NL spectra. However, linear simulations have been performed up to $k_y\rho_s \sim 2.5$ and the region $\sim 1 < k_y\rho_s < \sim 2$ has been found completely stable for both NBI and ICRH case, followed by a TEM-ETG branch that starts at $k_y\rho_s < \sim 2$, but which does not contribute to the NL fluxes. It is clear from figure 8 that the linear eigenvalues are similar when comparing the ICRH (solid red with squares) and NBI (solid black) cases. Also starting from the ICRH parameters and one by one substituting first the impurity parameters with the NBI ones (solid red with triangles), and then with the NBI FI (dashed red with triangles), just negligibly changes the spectrum. To further study the impact of the impurities, we recomputed the spectrum with GENE, removing the impurities (results shown for the ICRH case by a dashed blue line). The impurities are shown to moderately stabilize ITGs, but their impact is similar for ICRH and NBI cases, therefore changing the impurity parameters from ICRH to NBI ones does not impact the results. This is not unexpected since Z_{eff} is very similar for the two cases, as shown in figure 6. The FIs do not in practice change the spectrum.

As the second step, the electron particle flux dependence on its main driver R/L_n has been investigated for the ICRH case by means of a QL estimate based on linear GENE runs. An electrostatic (ES) 'mixing length' model has been adopted, following [53], based on the fact that '*a posteriori*' the nonlinear contribution to the nonlinear GENE fluxes coming from B fluctuations is found negligible with respect to the one coming from the ES potential fluctuations. The QL fluxes are obtained by weighting the outputs of GENE linear k_y scans with QL saturation amplitudes $w^{QL}(k_y) = [\gamma(k_y)/\langle k_\perp^2\rangle(k_y)]^\xi$, considering 3 k_x wavenumbers in the $\langle k_\perp^2\rangle$ computation and $\xi = 2$. The QL electron particle flux $\Gamma_e(k_y)$ spectrum (satisfying $\Gamma_e = \sum_{k_y}\Gamma_e(k_y)$), normalised with the sum of the heat fluxes divided by the temperature $(q_e + q_i)/T_e$, as a function of R/L_n is shown in figure 9. This normalized flux is useful when comparing GENE with the experiment, since if its agreement is good it is more likely that all the single fluxes Γ_e, q_e, q_i are in good agreement with the experiment. However, this could be due to a 'compensation of bad agreements', and therefore sometimes it is needed to look at the single fluxes, as will be shown in the following. In order to do that one needs NL simulations, which are able to compute the saturated values of the fluxes.

Figure 9 shows that the zero particle flux condition $\Gamma_e = 0$ (dashed magenta line), which is expected to be satisfied for

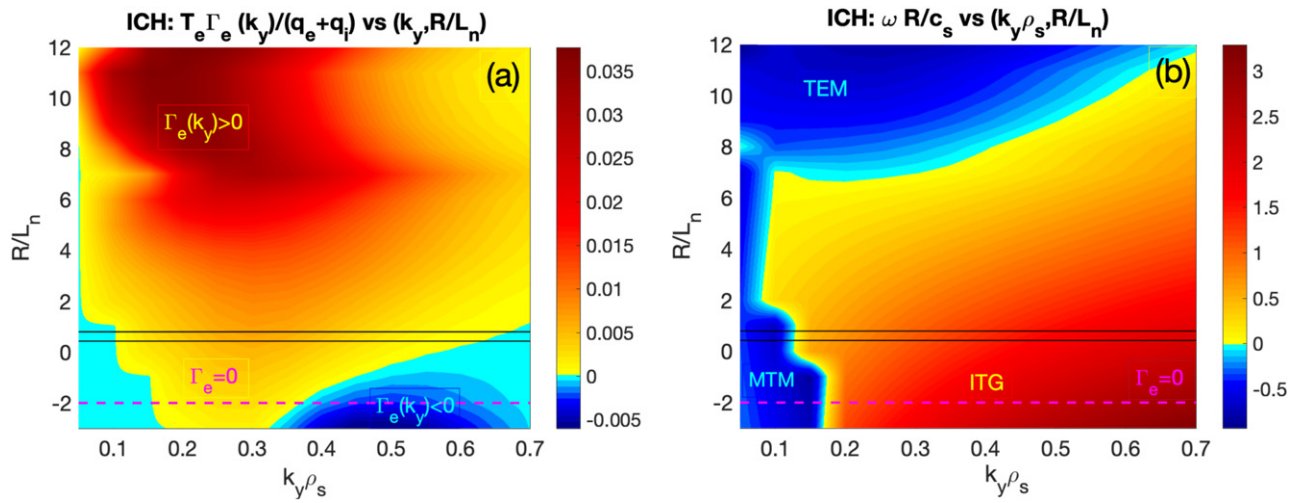

Figure 9. (*a*) QL estimate of the k_y spectrum of the electron particle flux Γ_e versus R/L_n, normalized with respect to $(q_e + q_i)/T_e$, for the ICRH case, where q_e and q_i are the QL estimates of the electron and ion heat fluxes respectively. (*b*) k_y spectrum of the frequency ω of the main unstable mode versus R/L_n. The horizontal solid black lines indicate the ICRH and NBI experimental R/L_n values, while the dashed magenta line shows the $\Gamma_e = 0$ condition.

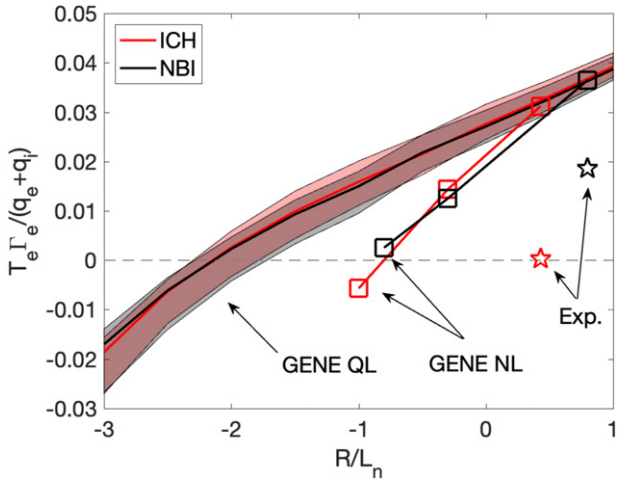

Figure 10. $T_e\Gamma_e/(q_e + q_i)$ versus R/L_n, comparing QL (solid lines with crosses (ICRH) and with triangles (NBI)), NL (squares), and experimental (stars) results, for the ICRH (red) and NBI (black) discharges.

the ICRH case at every radius due to lack of particle fueling, is in fact satisfied at smaller R/L_n (~ -2) than the experimental values of the ICRH and NBI discharges, shown as solid black lines in figure 9 (ICRH pulse has $R/L_n = 0.43$ and the NBI pulse has $R/L_n = 0.8$). Moreover, comparing figures 9(*a*) and 9(*b*), it is clear that both the simulated $R/L_n(\Gamma_e = 0)$ and the experimental R/L_n values lie in the ITG-dominant parameter region. In figure 9, the 'zero particle flux' condition is met by a spectral balance of an outward ITG particle flux coming from small binomial wavenumbers k_y, due to collisions ($\sim 0.15 < k_y\rho_s < \sim 0.35$) and an inward ITG flux from larger k_y ($\sim 0.35 < k_y\rho_s < \sim 0.7$) similarly to references [53, 54].

The results in figure 9(*a*) can be summed over the k_y spectrum, obtaining the QL total normalized electron particle flux $T_e\Gamma_e/(q_e + q_i)$ as a function of R/L_n. These results, together with the corresponding ones that have been obtained for the NBI case, are shown in figure 10 (ICRH: red, NBI: black, with error bars obtained by varying the parameters of the QL model, i.e. by changing $\xi = 1, 2, 3$ or by changing the number of radial wave numbers to be included in the $\langle k_\perp^2 \rangle$ computation; only $k_x = 0$ or 3 k_x values around $k_x = 0$ or all the k_x in the simulation grid), compared with the results of more realistic NL GENE runs (square markers, same color code) and with the experiment (stars). The NL simulations have been run with radial and binomial box sizes $[L_x, L_y] \sim [126, 80]\ \rho_s$ and $[n_{kx}, n_{ky}, n_z, n_{v\parallel}, n_\mu] = [15, 28, 32, 32, 48]$ typical number of grid points (x, y, z): field-aligned coordinate system in configuration space; ($v_\parallel$, μ): velocity variables in the reduced two-dimensional GK velocity space, covering only ion scales up to $k_y\rho_s < 1.6$. The $E \times B$ shearing is retained in the GENE NL simulations for the NBI case. This figure suggests that there is virtually no difference in the turbulent particle transport between the ICRH and NBI discharge, when considering the dependence of the normalized electron particle flux $T_e\Gamma_e/(q_e + q_i)$ on R/L_n. The QL results are in very good agreement with the NL ones at experimental mean parameters, while the agreement is worse at smaller (or negative) R/L_n, with QL data which underpredict the peaking with respect to NL ones. Indeed, the peaking factor $\mathrm{PF} = R/L_n(\Gamma_e = 0)$ is $\mathrm{PF} \sim -2$ for QL while it is $\mathrm{PF} \sim -1$ for NL. Both QL and NL results overestimate the experimental electron particle fluxes, especially for the ICRH case.

Additional NL GENE runs have been done to evaluate the nonlinear effect of $E \times B$ shearing, impurities and FI. This is illustrated in figure 11 and in the attached table. Starting with the parameters from the ICRH discharge, three additional NL runs have been done by substituting the impurities (blue), FI (light blue) or $E \times B$ shearing (red) from the NBI discharge, one by one to see their influence on the background transport. In the same spirit, starting with experimental data from the NBI discharge, an additional run has been done by removing the $E \times B$ shearing (to match the zero rotation of the ICRH pulse) to test its impact on the background transport. First, we can

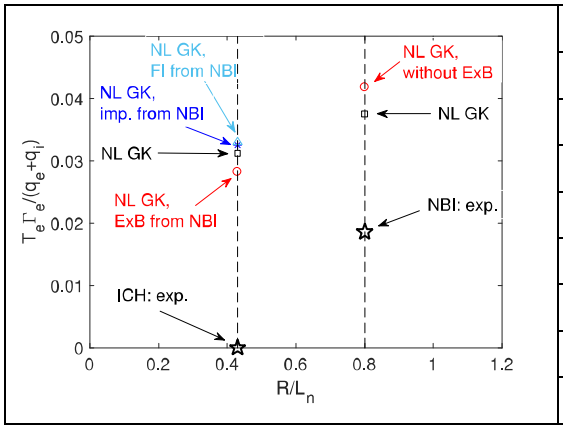

	$\Gamma_e[10^{19}s^{-1}m$	$q_e[kW\ m^{-2}]$	$q_i[kW\ m^{-2}]$	$T_e\Gamma_e/(q_e+q_i)$
ICRH: exp.	**~0**	**23.89**	**37.25**	**~0**
ICRH: GK	1.52	28.66	48.76	0.0312
ICRH: GK, imp. from NBI	1.65	29.70	50.43	0.0325
ICRH: GK, fast ions from NBI	1.80	32.17	54.49	0.0330
ICRH: GK, ExB from NBI	0.68	14.73	23.12	0.0282
NBI: exp.	**0.51**	**18.03**	**25.8**	**0.0186**
NBI: GK	0.74	11.78	19.36	0.0375
NBI: GK, without ExB	2.09	29.81	49.48	0.0418

Figure 11. Effect of the $E \times B$ shearing, impurities and FIs on the GK NL results, compared with experimental $T_e\Gamma_e/(q_e + q_i)$, using parameters from the ICRH (left vertical line) and NBI (right vertical line) discharges. The nominal ICRH pulse (black square) is compared with the one substituting the impurities from the NBI pulse (blue asterisk), or adding the FIs from NBI (light blue triangle), or finally adding $E \times B$ shearing from NBI (red circle). The nominal NBI pulse (black square) is compared with the one obtained removing the $E \times B$ shearing (red circle). On the right-hand side, the table displays the actual flux levels from the GK simulations and compared with the experiment.

look into the normalized electron particle flux (corresponding to the values of the last column of the table), observing that only the presence of the $E \times B$ shearing non-negligibly changes it, leading to slightly smaller values of $T_e\Gamma_e/(q_e + q_i)$. This could cause a tiny increase in the density peaking due to $E \times B$ shearing for the NBI case as also reported in [29], but as the rotation is relatively small with respect to typical JET H-mode plasmas with only 8 MW of NBI heating (central $v_{tor} = 110\ km\ s^{-1}$), the influence of $E \times B$ shearing on the peaking is expected to be small. However, looking into the absolute values of heat fluxes, it is evident that while the $E \times B$ shearing only slightly affects $T_e\Gamma_e/(q_e + q_i)$, its presence reduces the single fluxes by ~50%. The key point is that the reduction is similar for q_i, q_e and Γ_e (just a little bit larger for Γ_e), therefore probably the $E \times B$ shearing only affects the saturation levels of the potentials, thus the single flux variations balance out and $T_e\Gamma_e/(q_e + q_i)$ is only slightly lower when the $E \times B$ shearing is accounted for.

The GENE NL and QL results have been compared with the ones obtained with the stand-alone version of TGLF [45–47], using the two saturation models SAT1-geo (11/2019: an improved description of the geometrical effects with respect to SAT1 [55, 56]) and SAT2, providing a better fit of CGYRO results and an improved collisional model [57]. The same k_y grid that has been used in GENE is kept here for TGLF, covering the ion scales, to consistently compare the two codes. The results are shown in figure 12, where (*a*) corresponds to figure 10 and shows $T_e\Gamma_e/(q_e + q_i)$ vs R/L_n, while (*b*)–(*d*) shows the absolute fluxes Γ_e, q_e and q_i vs R/L_n in gyro-Bohm units, where $q_j\ [gB] = q_j/q_{norm,gB}$ (j = e, i and $q_{norm,gB} = \sqrt{m_i}n_eT_e^{5/2}/e^2R^2B_0^2$) and $\Gamma_e\ [gB] = \Gamma_e/\Gamma_{norm,gB}$ ($\Gamma_{norm,gB} = q_{norm,gB}/T_e$). The ICRH and NBI cases are indicated in red/black as in figure 10. GENE NL (squares) is compared with TGLF SAT1-geo (triangles) and TGLF SAT2 (circles). The crosses represent the results obtained from GENE simulations adding for the ICRH case the $E \times B$ shearing from the NBI one, and for the NBI case by removing the $E \times B$ shearing. The QL GENE results are shown in (*a*). Finally, the experimental values are indicated by stars. Before commenting the GENE-TGLF comparison, let us look at the GENE results alone. The GENE absolute fluxes (*b*)–(*d*) are singularly not so far from the experiment for the NBI case (q_e and q_i underestimate the experimental values by ~20%–30%, while Γ_e overestimate $\Gamma_{e,exp.}$ by ~40%), while for the ICRH case GENE largely overestimates (more than by a factor of 3 the $\Gamma_{e,exp.}$ of the NBI discharge) the experimental ~0 flux. Therefore, while for the ICRH case there is no agreement between GENE, which predicts a hollow n_e profile, and the experiment, for the NBI case GENE is approximately able to explain the experiment. This clearly demonstrates that the NBI particle source increases the peaking from negative (PF ~ −1, intersecting the GENE NL runs with $\Gamma_e \sim 0$) to positive, being thus the key player in setting the density peaking. Specifically, comparing (*a*) with (*b*)–(*d*), one sees that for the NBI case the large GENE overprediction of $T_e\Gamma_e/(q_e + q_i)$ case is mainly due to a moderate overprediction of Γ_e by GENE, while slightly underpredicting both q_e and q_i. The disagreement of the GENE results with the experimental ones for the ICRH case still remains to be explained.

Turning to the TGLF-GENE comparison, TGLF SAT1-geo almost perfectly agrees with GENE regarding the normalized $T_e\Gamma_e/(q_e + q_i)$ for both the NBI and ICRH cases. This is due to the good agreement on the values of all the single absolute fluxes Γ_e, q_e and q_i for the NBI case, while it is the result of a compensation of a TGLF underestimate of all the fluxes (in particular Γ_e and q_e) wrt. GENE for the ICRH case. The agreement of TGLF SAT2 with GENE is worse, since SAT2 predicts larger $T_e\Gamma_e/(q_e + q_i)$ for both NBI and ICRH cases. Specifically, SAT2 predicts a different R/L_n behavior with respect to GENE for all the fluxes, and well agrees with GENE at the experimental R/L_n only on q_e for the NBI case and on q_i for the ICRH case, while it always gives larger Γ_e than GENE NL. However, it is to be noted that SAT2 agrees with GENE on the general picture, predicting a negative peaking with $-2 <$ PF < -1.

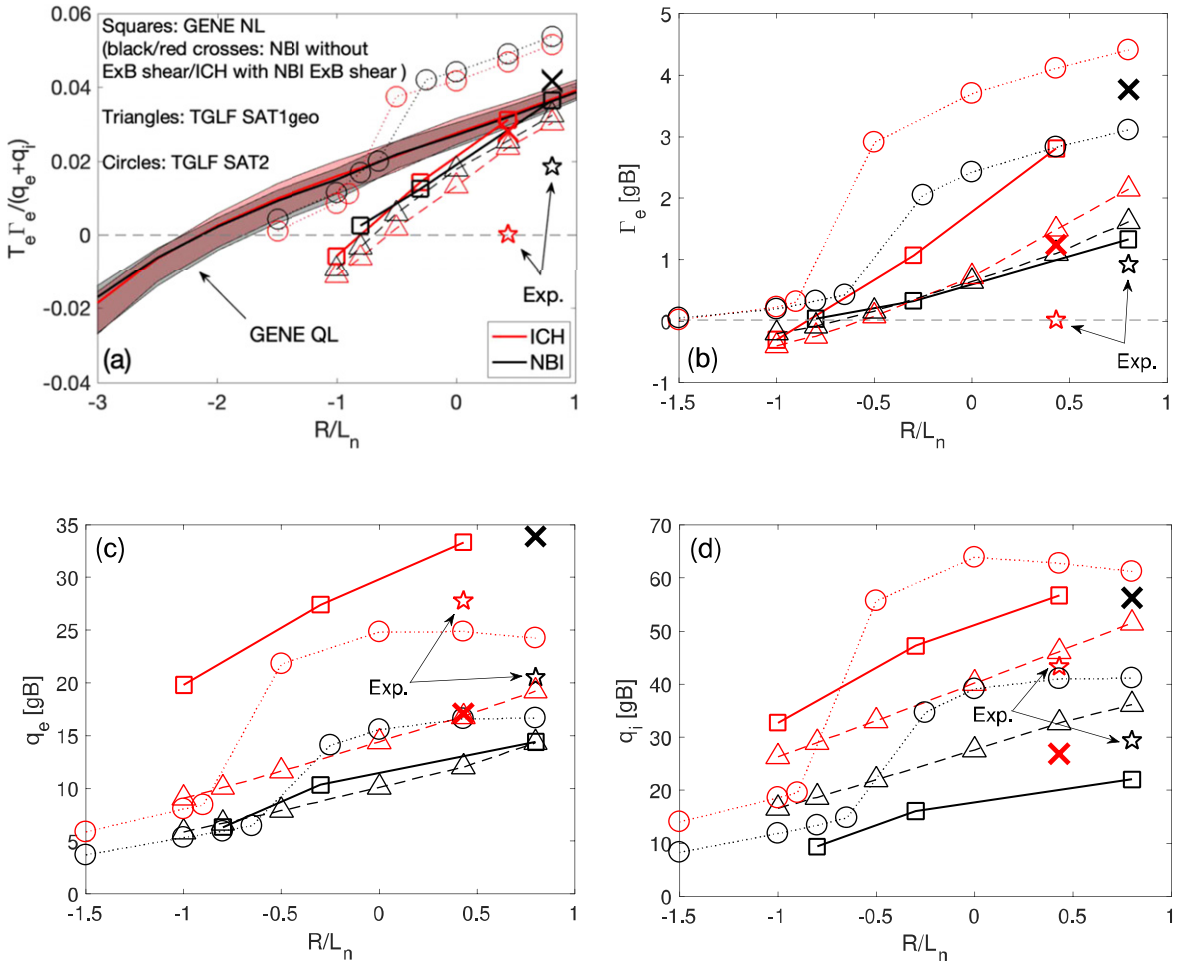

Figure 12. (*a*)–(*d*) $T_e\Gamma_e/(q_e+q_i)$, Γ_e[gB], q_e [gB] and q_i [gB] vs R/L_n for the ICRH (red) and NBI (black) cases, comparing GENE NL (squares) with the results obtained with the stand-alone versions of TGLF with the saturation models SAT1-geo (triangles) and SAT2 (circles). The crosses represent the results obtained by GENE adding for the ICRH case the $E\times B$ shearing from the NBI one and for the NBI case by removing the $E\times B$ shearing. The stars indicate the experimental values. In (*a*), the QL results are added.

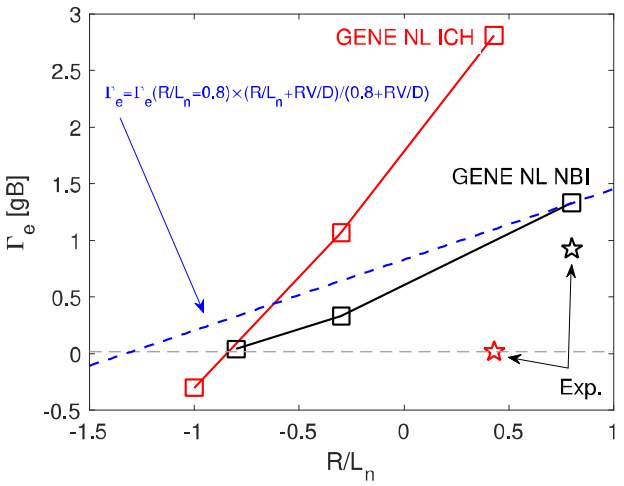

Figure 13. Γ_e [gB] vs R/L_n for the ICRH (red) and NBI (black) cases (corresponding to figure 11(*b*)), where for the NBI case a dashed blue line is added, showing the dependence of Γ_e [gB] on R/L_n when neglecting the dependence of D and V on R/L_n (with D and V values corresponding to the experimental $R/L_n = 0.8$).

To further test the picture of GENE predicting hollow n_e profile when not taking into account the NBI particle source for the NBI case, the electron particle diffusivity D and the electron particle convection V have been evaluated repeating the GENE NL simulation at experimental $R/L_n = 0.8$ for that case. We have added a passive electron species (also called 'tracer' species, which means that it does not affect the fluctuations of the scalar and vector potentials $\delta\phi$ and $\delta\mathbf{A}$, but it is affected by them) with $R/L_n = 0$. This way, since $\Gamma_e = (n_e/R)(DR/L_n + RV)$, it follows that D and V can be simply computed starting from the fluxes Γ_e and $\Gamma_{e,passive}$ of active and passive electrons as $D = (R/n_e)\,(\Gamma_e - \Gamma_{e,passive})/(R/L_n)$ and $V = \Gamma_{e,passive}/n_e$. The results, $D \simeq 0.18$ m s^{-1}, $V \simeq 0.08$ s^{-1}, indicate that there is an outward ($V > 0$) convection that contributes ~60% of the total electron particle flux Γ_e. This implies that a negative peaking given by PF$=R/L_n(\Gamma_e=0) \simeq -RV/D \simeq -1.33$ is expected, where this estimate neglects a possible dependence of D and V on R/L_n. This is not far from the predicted PF $\simeq -1$ from the GENE NL R/L_n scan, which retains the dependence of D and V on

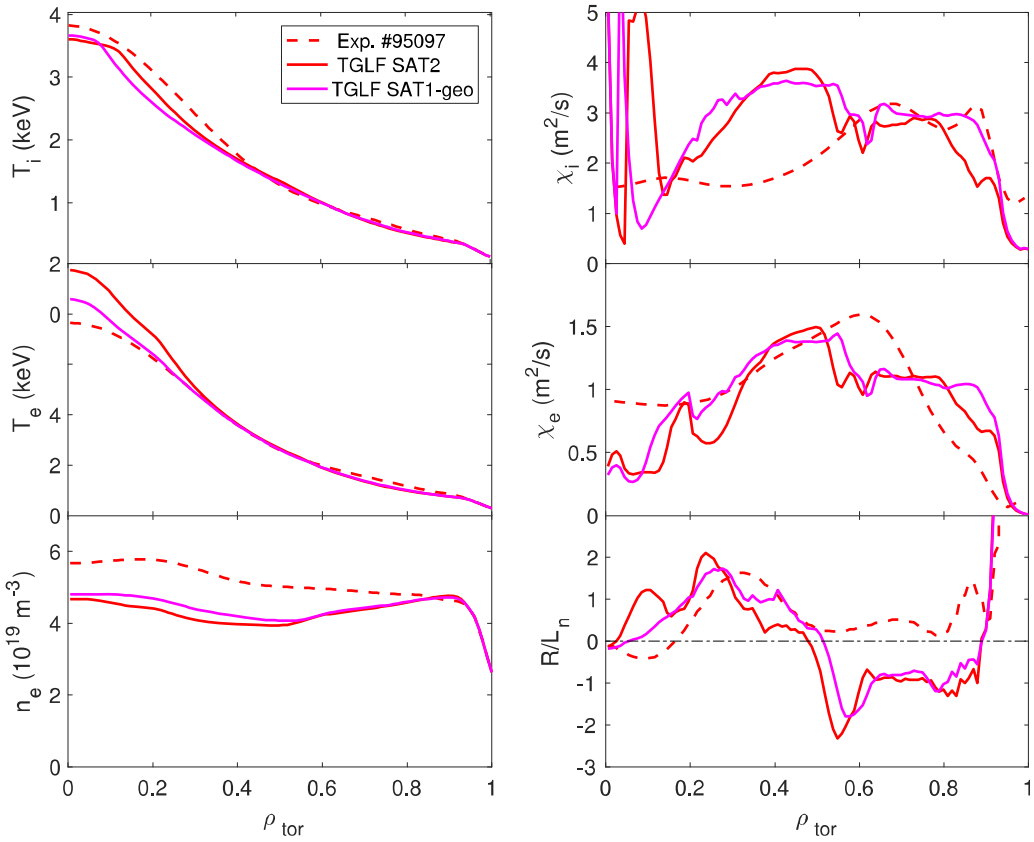

Figure 14. TGLF simulations of the ICRH discharge No. 95097. Shown from top to bottom are the ion temperature, the electron temperature and the electron density profiles (left frame) and the ion and electron diffusivities and the inverse of the normalized density length, respectively (right frame).

R/L_n. The difference of the dependence of Γ_e vs R/L_n that is observed retaining/neglecting the dependence of D and V on R/L_n can be better visualized comparing the black/blue lines in figure 13, where the blue line shows $\Gamma_e = \Gamma_e(R/L_n = 0.8) \times (R/L_n + RV/D)/(0.8 + RV/D)$, keeping PF $= RV/D =$ const. $= -1.33$.

Summarizing the results of the local analysis at $\rho_{tor} = 0.6$, consisting of GENE and TGLF stand-alone simulations, the main outcome is that for the NBI pulse the NBI particle source is the main player in setting the n_e peaking. Without considering the NBI source, both GENE and TGLF predict a negative PF, corresponding to a locally hollow n_e profile. Neither TGLF nor GENE is able to reproduce the positive peaking for the ICRH case, predicting a hollow n_e profile, due to an outward turbulent convection and experimental $\sim$0 particle source. This remains a mystery and it is left for future work. A comparison of the turbulent transport between the NBI and ICRH cases, evaluating the impact of impurities, FI and toroidal rotation, which are the only significant experimental differences, shows that only the $E \times B$ shearing, associated with the toroidal rotation produced by the NBI, stabilizes the absolute fluxes for the NBI case, but only slightly affects the normalized Γ_e. Therefore, it virtually does not change the peaking given by the zero particle flux condition (PF), which is obtained by neglecting the particle source, i.e. by considering only the turbulent diffusion and convection.

To explore the radial dependence of the results, predictive integrated transport simulations with the ASTRA transport code have been performed for both ICRH and NBI cases. The results obtained using TGLF with the two saturation models SAT2 and SAT1-geo are compared. The boundary conditions are taken at $\rho_{tor} = 0.94$ for both ICRH and NBI cases, and the simulations include electromagnetic ($B_\perp$) and $E \times B$ shear effects. The simulations solve the electron and ion heat transport equations and the electron particle transport equation while the profiles of toroidal rotation, impurities (Z_{eff}), radiation and q-profile are prescribed from the experiments. The equilibrium is taken from EFIT with pressure constraints and the simulations are long enough to reach the steady-state, typically around 1 s long, i.e. 5–10 energy confinement times. The NBI and ICRH heating and fuelling profiles are as described in section 3. TGLF is called with four kinetic species (electrons, ions, beryllium and a heavy impurity lumping the nickel and tungsten). FI dilution is also taken into account.

The results of the ASTRA-TGLF runs are presented in figures 14 and 15 for the ICRH and NBI case, respectively. The simulations (solid) are compared with the experiment (dashed). For the NBI case, an additional ASTRA-TGLF SAT2 simulation where the NBI particle source has been switched off is added (dotted), to evaluate its impact. The temperature profiles are well predicted for both the ICRH and NBI cases, in particular between $\rho_{tor} = 0.4$ and $\rho_{tor} = 0.8$, which is the main interest here. The experimental n_e profiles, on the contrary, are

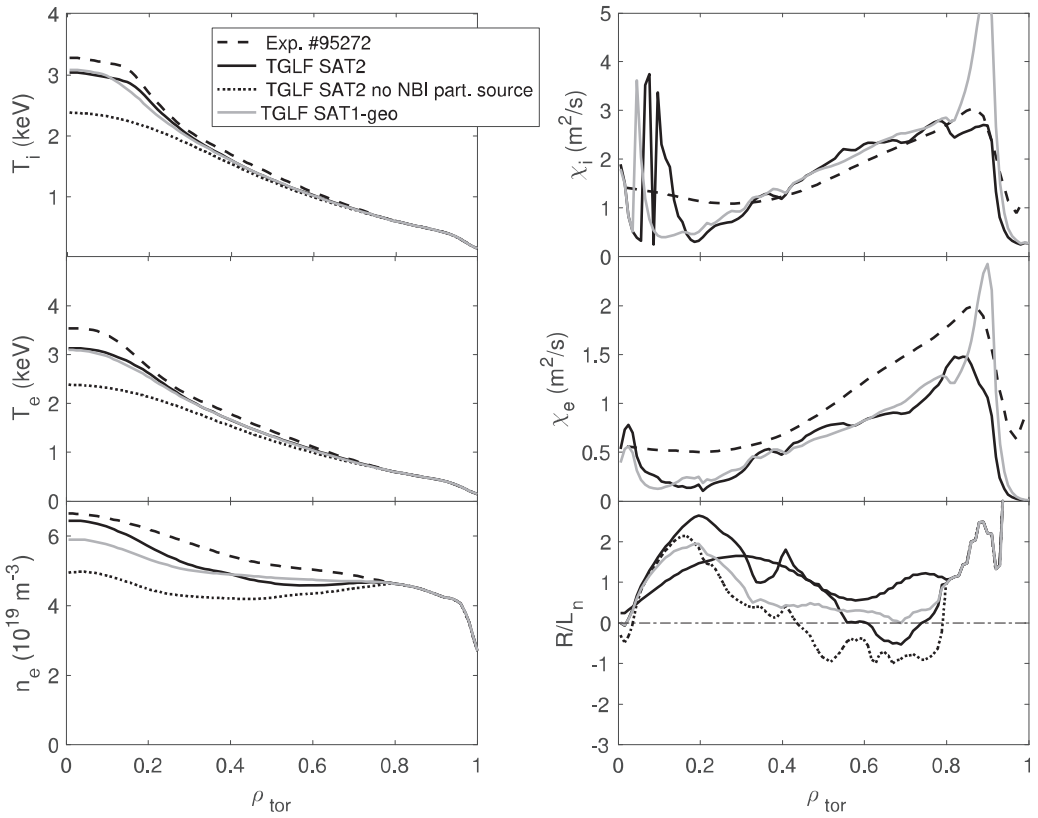

Figure 15. TGLF simulations of the NBI discharge No. 95272. Shown from top to bottom are the ion temperature, the electron temperature and the electron density profiles (left frame) and the ion and electron diffusivities and the inverse of the normalized density length, respectively (right frame).

underpredicted by the simulations. In particular, for the ICRH case, n_e is strongly underpredicted by ASTRA, which manifests itself as a negative peaking with $-2 < \mathrm{PF} < -1$ for $0.5 < \rho_{tor} < 0.8$, in agreement with the local analysis at $\rho_{tor} = 0.6$. For the NBI case, taking into account the NBI source reverses the n_e peaking in the region $0.5 < \rho_{tor} < 0.8$ from hollow to almost flat, or even positive if we consider ASTRA-TGLF SAT1-geo that gives a prediction that is approaching the experimental density profile. The two saturation models SAT2 and SAT1-geo give similar results when looking at the heat transport, while SAT1-geo better agrees with the experiment regarding the n_e peaking prediction, especially for the NBI case. This reflects the better agreement of TGLF stand-alone with GENE when using SAT1-geo model at $\rho_{tor} = 0.6$.

5. Conclusions and future work

The ICRH versus NBI identity plasmas in JET show that the NBI fuelled discharge has a factor of 2 higher density peaking ($R/L_n = 0.93$ for the NBI shot and $R/L_n = 0.45$ for the ICRH shot). The dimensionless profiles of $q, \rho^*, \nu^*, \beta_n$ and $T_i/T_e \approx 1$ were matched within 5% accuracy except in the central part of the plasma ($\rho_{tor} < 0.3$), yielding similar plasma parameters and performance in the confinement region ($0.3 < \rho_{tor} < 0.8$). We had succeeded to minimize the difference in the curvature pinch (same q-profile) and thermo-pinch ($T_{ICRH} = T_{NBI}$) between the ICRH and NBI shots, simplifying greatly our main task to quantify the magnitude of the NBI fuelling. The key question in this paper was to clarify whether the influence of the NBI fuelling on density peaking is exactly or closely the observed factor of 2 under these identity plasma conditions.

In addition to different density peaking, the four other main experimental differences between the ICRH and NBI plasmas were the toroidal rotation, plasma FI density and energy, the heavy impurity densities of tungsten and nickel, and the radiated power. The impact of these on density peaking were thoroughly investigated GENE and ASTRA/TGLF modelling. The main conclusions from both the GK GENE simulations, the QL simulations with the stand-alone version of TGLF and the ASTRA predictive transport modelling with TGLF all strongly support the experimental result where the NBI fuelling is the main contributor to the density peaking with respect to the non-fuelled ICRH identity plasma. The simulations results can be summarized as follows: (1) the dependence of the normalized turbulent electron particle flux on the logarithmic density gradient is similar for the ICRH and NBI discharges at $\rho_{tor} = 0.6$, giving similar negative peaking when neglecting the NBI particle source for the NBI case; (2) the NBI source is thus the main player in setting the n_e peaking for the NBI case, allowing it to increase from negative to positive, close to the experiment. This holds for $0.5 < \rho_{tor} < 0.8$

according to ASTRA-TGLF runs. (3) A positive electron particle convection (outward convection) is found at $\rho_{tor} = 0.6$ for the NBI case by GENE NL. This confirms that without the NBI source the predicted density peaking would be negative. (4) Both GENE and TGLF predict hollow n_e for the ICRH case, in contrast with the experiment. This should be investigated in future; (5) the FI and impurity content differ between the two pulses, but they do not to impact the turbulence at $\rho_{tor} = 0.6$. Only the $E \times B$ shearing due to the toroidal rotation that is induced by the NBI affects the turbulence, stabilizing all the fluxes. However, it seems to only impact the saturation values of the potentials, affecting all the fluxes in approximately the same way, and therefore it has a minor impact on the density peaking; (6) TGLF SAT1-geo is slightly better than SAT2 when predicting the n_e profile, especially for the NBI case.

We can conclude based on the ICRH-NBI identity discharge pair that the NBI particle source is the main player in contributing to the density peaking for the NBI pulse, and therefore the NBI source is the best candidate to explain the double peaking that is observed in the NBI pulse with respect to the ICRH one. This experimental result of R/L_n increasing roughly by a factor of 2 per 8 MW of NBI power and fueling with respect to non-fueled ICRH discharge is valid for low power JET H-mode plasmas dominated by the ITG turbulence. It is to be noted here that some of the physics processes affecting particle transport, like turbulence type, toroidal rotation and FI content scale with the heating power and consequently, the conclusions on the contribution of the NBI fueling on density peaking may differ for higher power JET plasmas. However, it is important to remember that ITG has been found to be the dominant turbulence type in either low power or high NBI power JET plasmas. Therefore, although this kind of ICRH-NBI identity pulse pair cannot be performed in JET high power conditions due to lack of the required ICRH power, the significant role played by the NBI fueling in contributing to density peaking seems very much plausible. There is in fact evidence on that, reported in reference [12] based on density peaking in the JET three-point dimensionless collisionality scan. However, there is also evidence that as the ITG turbulence is less dominant or in other words when TEM dominates, the role of NBI fueling in contributing to density peaking tends to decrease which have been published in references [13, 14].

An additional experiment will be executed in JET to study how particle transport will scale when changing the hydrogen isotope. The plan is to execute a similar identity experiment to this paper, but using 8 MW of NBI heating/fuelling in pure 100% tritium plasma. We will be able to document both the isotope scaling of the dependence of density peaking on NBI fuelling and the role NBI fuelling with NBI system in tritium in JET tritium versus deuterium plasma, by adopting the same experimental conditions as reported in this paper. Moreover, we will study the isotope scaling of particle transport and density peaking between tritium and deuterium pulses, including both the dimensionless and dimensional identity conditions in JET L-mode plasma.

Acknowledgments

'This work has been carried out within the framework of the EUROfusion Consortium and has received funding from the Euratom research and training programme 2014–2018 and 2019–2020 under Grant Agreement No. 633053. The views and opinions expressed herein do not necessarily reflect those of the European Commission'.

ORCID iDs

T. Tala https://orcid.org/0000-0002-6264-0797
F. Eriksson https://orcid.org/0000-0002-2740-7738
P. Mantica https://orcid.org/0000-0001-5939-5244
A. Mariani https://orcid.org/0000-0003-0476-3825
E.R. Solano https://orcid.org/0000-0002-4815-3407
J. Ferreira https://orcid.org/0000-0001-5015-7207
E. Fransson https://orcid.org/0000-0002-8747-3470
L. Horvath https://orcid.org/0000-0002-5692-6772
C. Maggi https://orcid.org/0000-0001-7208-2613
R.B. Morales https://orcid.org/0000-0003-0667-3356
C. Perez von Thun https://orcid.org/0000-0002-1166-2179
P.A. Schneider https://orcid.org/0000-0001-7257-3412

References

[1] Maisonnier D. *et al* 2005 *Fusion Eng. Des.* **75–79** 1173
[2] Angioni C., Fable E., Greenwald M., Maslov M., Peeters A.G., Takenaga H. and Weisen H. 2009 *Plasma Phys. Control. Fusion* **51** 124017
[3] Weisen H., Zabolotsky A., Garbet X., Mazon D., Zabeo L., Giroud C., Leggate H., Valovic M. and Zastrow K.-D. (JET-EFDA Workprogramme) 2004 *Plasma Phys. Control. Fusion* **46** 751
[4] Valovič M. *et al* 2004 *Plasma Phys. Control. Fusion* **46** 1877
[5] Angioni C. *et al* 2007 *Nucl. Fusion* **47** 1326–35
[6] Weisen H., Zabolotsky A., Maslov M., Beurskens M., Giroud C. and Mazon D. (JET-EFDA Contributors) 2006 *Plasma Phys. Control. Fusion* **48** A457
[7] Greenwald M., Angioni C., Hughes J.W., Terry J. and Weisen H. 2007 *Nucl. Fusion* **47** L26–9
[8] Valovič M., Garzotti L., Voitsekhovitch I., Beurskens M., Garbet X., Giroud C. and Keeling D. 2007 *Nucl. Fusion* **47** 196
[9] Garzotti L., Valovič M., Garbet X., Mantica P. and Parail V. (JET-EFDA Contributors) 2006 *Nucl. Fusion* **46** 994
[10] Fable E., Angioni C. and Sauter O. 2010 *Plasma Phys. Control. Fusion* **52** 015007
[11] Maslov M., Angioni C. and Weisen H. 2009 *Nucl. Fusion* **49** 075037
[12] Tala T. *et al* 2019 *Nucl. Fusion* **59** 126030
[13] Mordijck S. *et al* 2020 *Nucl. Fusion* **60** 066019
[14] Fable E. *et al* 2019 *Nucl. Fusion* **59** 076042
[15] Salmi A. *et al* ((JET Contributors) 2018 *45th EPS Conf.* (Prague, Czech Republic 2–6 July 2018) p P4.1068 (http://ocs.ciemat.es/EPS2018PAP/pdf/P4.1068.pdf)
[16] Gentle K.W., Gehre O. and Krieger K. 1992 *Nucl. Fusion* **32** 217
[17] Sips A.C.C. and Kramer G.J. 1993 *Plasma Phys. Control. Fusion* **35** 743

[18] Baker D.R., Wade M.R., Jackson G.L., Maingi R., Stockdale R.E., deGrassie J.S., Groebner R.J., Forest C.B. and Porter G.D. (DIII-D Team) 1998 *Nucl. Fusion* **38** 485
[19] Koponen J.P.T. *et al* 2000 *Nucl. Fusion* **40** 365
[20] Tanaka K. *et al* 2006 *Nucl. Fusion* **46** 110
[21] Frassinetti L., Beurskens M.N.A., Scannell R., Osborne T.H., Flanagan J., Kempenaars M., Maslov M., Pasqualotto R. and Walsh M. 2012 *Rev. Sci. Instrum.* **83** 013506
[22] Maslov M. *et al* 2018 *Nucl. Fusion* **58** 076022
[23] Bourdelle C., Camenen Y., Citrin J., Marin M., Casson F.J., Koechl F. and Maslov M. 2018 *Nucl. Fusion* **58** 076028
[24] Versloot T.W. *et al* 2011 *Nucl. Fusion* **51** 103033
[25] McDermott R.M., Angioni C., Dux R., Gude A., Pütterich T., Ryter F. and Tardini G. 2011 *Plasma Phys. Control. Fusion* **53** 035007
[26] Sommer F. *et al* 2012 *Nucl. Fusion* **52** 114018
[27] Sommer F. *et al* 2015 *Nucl. Fusion* **55** 033006
[28] Wang X. *et al* 2016 *Plasma Phys. Control. Fusion* **58** 045026
[29] Garcia J., Doerk H. and Görler T. 2019 *Plasma Phys. Control. Fusion* **61** 104002
[30] Eriksson F., Oberparleiter M., Skyman A., Nordman H., Strand P., Salmi A. and Tala T. 2019 *Plasma Phys. Control. Fusion* **61** 075008
[31] Jacquet P. *et al* 2017 *EPJ Web Conf.* **157** 02004
[32] Ciric D. *et al* 2007 *Fusion Eng. Des.* **82** 610–8
[33] Giroud C. *et al* 2008 *Rev. Sci. Instrum.* **79** 525
[34] Ho A., Citrin J., Auriemma F., Bourdelle C., Casson F.J., Kim H.-T., Manas P., Szepesi G. and Weisen H. 2019 *Nucl. Fusion* **59** 056007
[35] (https://transp.pppl.gov) (https://doi.org/10.11578/dc.20180627.4)
[36] Goldston R.J., McCune D.C., Towner H.H., Davis S.L., Hawryluk R.J. and Schmidt G.L. 1981 *J. Comput. Phys.* **43** 61
[37] Pankin A., McCune D., Andre R., Bateman G. and Kritz A. 2004 *Comput. Phys. Commun.* **159** 157–84
[38] Eriksson L.-G., Hellsten T. and Willen U. 1993 *Nucl. Fusion* **33** 1037
[39] Brambilla M. 1999 *Plasma Phys. Control. Fusion* **41** 1
[40] Romanelli M. *et al* 2014 *Plasma Fusion Res.* **9** 3403023
[41] Sertoli M. *et al* 2018 *Rev. Sci. Instrum.* **89** 113501
[42] Sertoli M., Carvalho P.J., Giroud C. and Menmuir S. 2019 *J. Plasma Phys.* **85** 905850504
[43] Houlberg W.A., Shaing K.C., Hirshman S.P. and Zarnstorff M.C. 1997 *Phys. Plasmas* **4** 3230
[44] Jenko F., Dorland W., Kotschenreuther M. and Rogers B.N. 2000 *Phys. Plasmas* **7** 1904
[45] Staebler G.M., Kinsey J.E. and Waltz R.E. 2005 *Phys. Plasmas* **12** 102508
[46] Staebler G.M., Kinsey J.E. and Waltz R.E. 2007 *Phys. Plasmas* **14** 055909
[47] Staebler G.M., Candy J., Waltz R.E., Kinsey J.E. and Solomon W.M. 2013 *Nucl. Fusion* **53** 113017
[48] Pereverzev G.V. and Yushmanov P.N. 2002 ASTRA automated system for transport analysis in a tokamak *IPP Report 5/98* (Max-Planck-Institut für Plasmaphysik)
[49] Mariani A., Mantica P., Casiraghi I., Citrin J., Görler T. and Staebler G.M. (EUROfusion JET1 Contributors) 2021 *Nucl. Fusion* **61** 066032
[50] Lao L.L., John H.S., Stambaugh R.D. and Pfeiffer W. 1985 *Nucl. Fusion* **25** 1421
[51] Brix M., Hawkes N.C., Boboc A., Drozdov V. and Sharapov S.E. 2008 *Rev. Sci. Instrum.* **79** 10F325
[52] Miller R.L., Chu M.S., Greene J.M., Lin-Liu Y.R. and Waltz R.E. 1998 *Phys. Plasmas* **5** 973
[53] Mariani A., Brunner S., Dominski J., Merle A., Merlo G., Sauter O., Görler T., Jenko F. and Told D. 2018 *Phys. Plasmas* **25** 012313
[54] Angioni C. *et al* 2009 *Phys. Plasmas* **16** 060702
[55] Staebler G.M., Candy J., Howard N.T. and Holland C. 2016 *Phys. Plasmas* **23** 062518
[56] Staebler G.M., Howard N.T., Candy J. and Holland C. 2017 *Nucl. Fusion* **57** 066046
[57] Staebler G.M., Candy J., Belli E.A., Kinsey J.E., Bonanomi N. and Patel B. 2021 *Plasma Phys. Control. Fusion* **63** 015013